Exciton–phonon coupling strength in single-layer $MoSe_2$ at room temperature

Donghai Li[1], Chiara Trovatello[2], Stefano Dal Conte[2], Matthias Nuß[1], Giancarlo Soavi[3,4], Gang Wang[3], Andrea C. Ferrari[3], Giulio Cerullo[2,5*] and Tobias Brixner[1,6*]*

[1]Institut für Physikalische und Theoretische Chemie, Universität Würzburg, Am Hubland, 97074 Würzburg, Germany

[2]Dipartimento di Fisica, Politecnico di Milano, Piazza L. da Vinci 32, I-20133 Milano, Italy

[3]Cambridge Graphene Centre, University of Cambridge, 9 JJ Thomson Avenue, Cambridge CB3 0FA, UK

[4]Institute for Solid State Physics, Abbe Center of Photonics, Friedrich-Schiller-University Jena, Max-Wien-Platz 1, 07743, Jena, Germany

[5]IFN-CNR, Piazza L. da Vinci 32, I-20133 Milano, Italy

[6]Center for Nanosystems Chemistry (CNC), Universität Würzburg, Theodor-Boveri-Weg, 97074 Würzburg, Germany

[*]e-mails: acf26@eng.cam.ac.uk, giulio.cerullo@polimi.it, brixner@uni-wuerzburg.de

Single-layer transition metal dichalcogenides (1L-TMDs) are at the center of an ever increasing research effort both in terms of fundamental physics and applications. Exciton–phonon coupling (EXPC) plays a key role in determining the photonic and (opto)electronic properties of 1L-TMDs. However, the EXPC strength has not been measured at room temperature. Here, we develop two-dimensional (2D) micro-spectroscopy to determine EXPC of 1L-$MoSe_2$. We detect beating signals as a function of waiting time *T*, induced by

the coupling between the A exciton and the A'$_1$ optical phonon. Analysis of 2D beating maps provides the EXPC with the help of simulations. The Huang–Rhys factor of ~1 is larger than in most other inorganic semiconductor nanostructures. Our technique offers a unique tool to measure EXPC also in other 1L-TMDs and heterogeneous semiconducting systems with a spatial resolution ~260 nm, and will provide design-relevant parameters for the development of novel optoelectronic devices.

Layered materials (LMs)[1–4], such as single-layer (1L) transition metal dichalcogenides (1L-TMDs)[5–8], are a promising platform for new photonic and optoelectronic devices. Bulk semiconducting TMDs consist of covalently bound layers of the type MX_2, where M is a metal (e.g., Mo, W) and X is a chalcogen atom (e.g., S, Se), held together by van der Waals interactions[3]. When they are exfoliated or grown as 1L, quantum confinement induces an indirect-to-direct bandgap transition[5,6]. The reduced dimensionality is also responsible for high exciton binding energies (hundreds of meV)[7,8], making 1L-TMDs excellent candidates for optoelectronic devices at room temperature (RT)[2].

Exciton–phonon coupling (EXPC) plays a key role in determining the T-dependent optoelectronic and transport properties of 1L-TMDs[9–11]. It is responsible for, e.g., non-radiative exciton decay[9,10,12], limiting the fluorescence quantum yield[13], the formation of dark-exciton phonon replicas[14], and it mediates spin-flip processes, thus decreasing the lifetime of spin/valley-polarized charge carriers[15]. For T<100 K, the interaction between excitons and acoustic phonons induces linewidth broadening and dominates the excitonic resonance of 1L-TMDs[9,16,17]. While this interaction is well understood, the situation is different for higher T. Ref. 18 suggested that the coupling between excitons and optical phonons induces sidebands in the absorption spectrum of 1L-$MoSe_2$ at RT. Yet the spectral signature of this coupling is obscured by inhomogeneous broadening[18]. The presence of EXPC was inferred from resonance Raman scattering[19,20] as well as time-resolved transmission measurements[21,22],

where the A'_1 optical phonon mode was observed to couple with the A excitonic resonance. While the energetic position of excitons can be obtained from photoluminescence and the energetic position of (ground-state) phonons from Raman measurements, this does not fully characterize the system. For obtaining the complete Hamiltonian, one also requires the displacement along the phonon coordinate of the exciton-state potential energy minimum versus the ground state. This displacement is the EXPC strength, as further detailed below, that determines how strongly phonons will be excited upon an optical transition to the exciton state. To the best of our knowledge, the EXPC strength has never been determined for any 1L-TMD at room temperature, because overtone bands of the optical phonon mode were not detectable[19–22], and thus the optical characterization of this (and similar) material(s) is incomplete. We determine the missing quantity in the present work.

Optical four-wave-mixing experiments in semiconductors provide access to coherent dynamics of excitons[23–25,10]. In photon echo experiments the polarization state of incident photons (circular or linear) allows one to uncover different mechanisms behind the signal formation[26,27]. Different level schemes can be distinguished by the polarization dependence[27]. Two-dimensional electronic spectroscopy (2DES) is a powerful tool to analyze light-induced coherences in molecular systems[28–31] and semiconductors[32,33]. It is a generalized version of transient absorption spectroscopy, providing frequency resolution not only for the probe step, but also for the pump[34–38]. Coherent broadband excitation of several quantum energy levels leads to wave packets that may be detected as oscillations of specific peaks in the 2D maps as a function of waiting time T[29,39]. Analysis of frequency, decay time, and the position of such oscillations allows one to explore the underlying energy structure and the coupling mechanism leading to level splittings[29,39,40].

It is challenging to apply 2DES on micro-scale samples or heterogeneous materials with localized structural domains on a μm lateral scale, because the standard phase-matching geometry requires the exciting beams to be non-collinear with respect to each other[36]. This

cannot be realized simultaneously when focusing with a high-numerical-aperture (high-NA) objective, in which all incident light arrives from the same solid angle at the sample. As a result, if one chooses to employ phase matching, this necessarily requires longer focal lengths, leading to larger spot sizes and unwanted averaging over different spatial regions or crystal orientations[41]. Instead, one can also select the signal by phase cycling[42–44], which relies on detecting population-based signals as a function of inter-pulse phase combinations[42,44,45]. The collinear geometry accessible with phase cycling enables 2D micro-spectroscopy, i.e., the combination of 2DES with fluorescence microscopy, to gain additional spatial resolution[41,46].

Here, we develop 2D micro-spectroscopy to resolve the spectral features of the phonon sidebands in 1L-$MoSe_2$ at RT and determine the EXPC. We observe oscillations in 2D maps that arise from the coupling between the A'_1 optical phonon mode and the A exciton. From comparison with simulated 2D beating maps, we deduce a Huang–Rhys factor, S~1. This implies a large EXPC strength for 1L-$MoSe_2$, when compared with other inorganic semiconductor nanostructures, such as CdSe quantum dots[47] and rods[48], ZnSe quantum dots[49], single-wall carbon nanotubes[50], etc., most of which fall in the range of 0–0.5 [51], providing design-relevant information for the development of photonic devices based on 1L-$MoSe_2$. Our method can be extended to other 1L-TMDs and materials and, additionally, also to other important semiconducting systems, for which the ~260-nm spatial resolution of the 2D micro-spectroscopy is required, e.g., single-wall carbon nanotubes, van-der-Waals heterostructures of layered materials, layered perovskites, bulk heterojunctions, or microcavities with embedded semiconductors.

Results and discussion

The experimental setup is sketched in Fig. 1a. A Ti:sapphire oscillator emits 12-fs pulses at 80 MHz repetition rate. A pulse shaper generates a collinear four-pulse sequence, focused by a high-NA objective (NA = 1.4), so that a spatial resolution~260 nm is achieved. To image

the sample, the laser focus is mapped by a piezo scanning stage, and the photoluminescence (PL) signal is detected by an avalanche photodiode (APD). For the 2D map, the PL intensity is detected while scanning a first coherence time τ (delay between the first two pulses), a waiting time T (delay between the second and the third pulses), and a second coherence time t (delay between the third and the fourth pulses, Fig. 1a). Fourier transformation over τ and t results in a 2D map for every T (see Methods for data acquisition details). Nonlinear signals are obtained by systematically scanning through a number of discrete phase steps for each pulse and for each pulse-delay combination, and rephasing and nonrephasing signals are retrieved as linear superpositions of differently phase-modulated data[44].

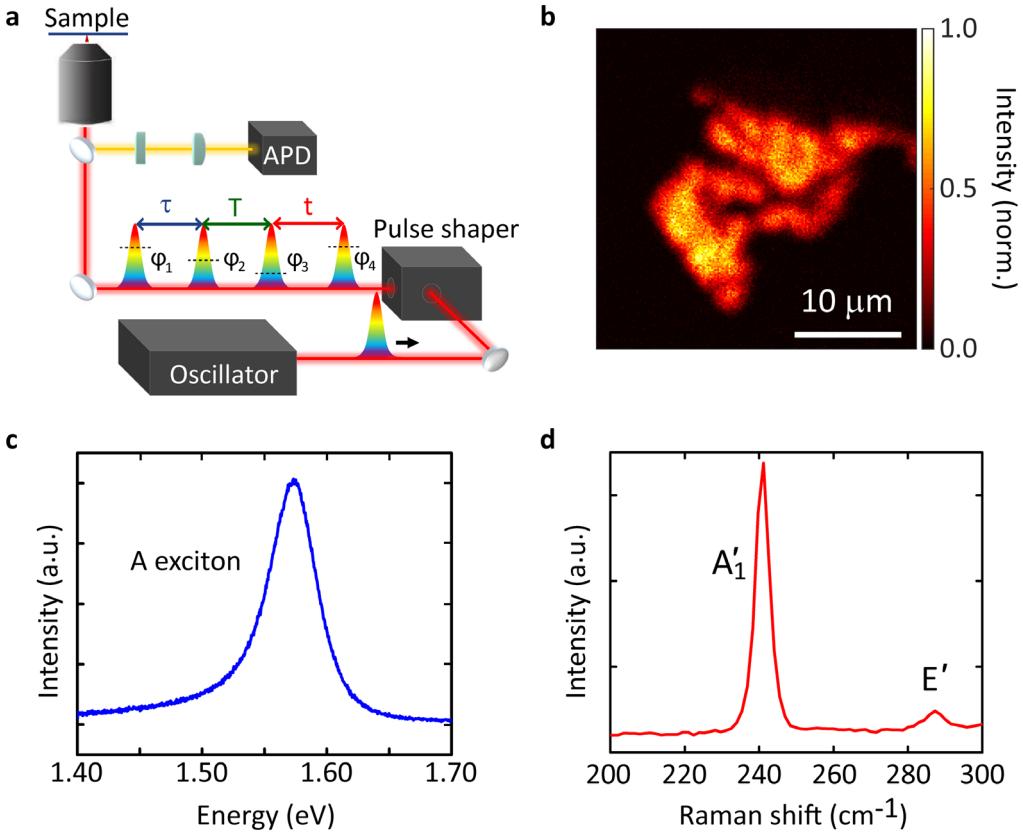

Figure 1 | Overview of setup and the sample. a, Fluorescence-detected 2D micro-spectroscopy setup. Four collinear laser pulses are generated by a pulse shaper with controllable inter-pulse time delays (τ, T, t) and phases (ϕ_i, i = 1, 2, 3, 4) and focused by a high-NA objective (Obj). The position of the sample is controlled by a piezo scanning stage (PSS). The PL signal is detected by an avalanche photodiode (APD). **b,** PL map obtained with the setup of panel **a**. **c,** PL and **d,** Raman spectrum for 514 nm excitation.

We investigate mechanically exfoliated 1L-$MoSe_2$ on a 200 μm fused silica substrate (see Methods for details). Figure 1b is a PL map, taken with the setup of Fig. 1a, for a representative sample. 1L-$MoSe_2$ has a direct bandgap at the K point of the Brillouin zone leading to two excitonic transitions A and B ~1.57 and 1.75 eV[52]. The PL spectrum (Fig. 1c) shows a single peak ~1.57 eV, due to the radiative recombination of A excitons[53]. The Raman spectrum measured at 514 nm (Fig. 1d) shows the out-of-plane A'_1 mode ~241 cm^{-1} with full width at half maximum (FWHM) ~4 cm^{-1}, and the in-plane E' mode ~288 cm^{-1} (FWHM ~6 cm^{-1}). Both PL and Raman spectra confirm that the sample is 1L-$MoSe_2$[53,19].

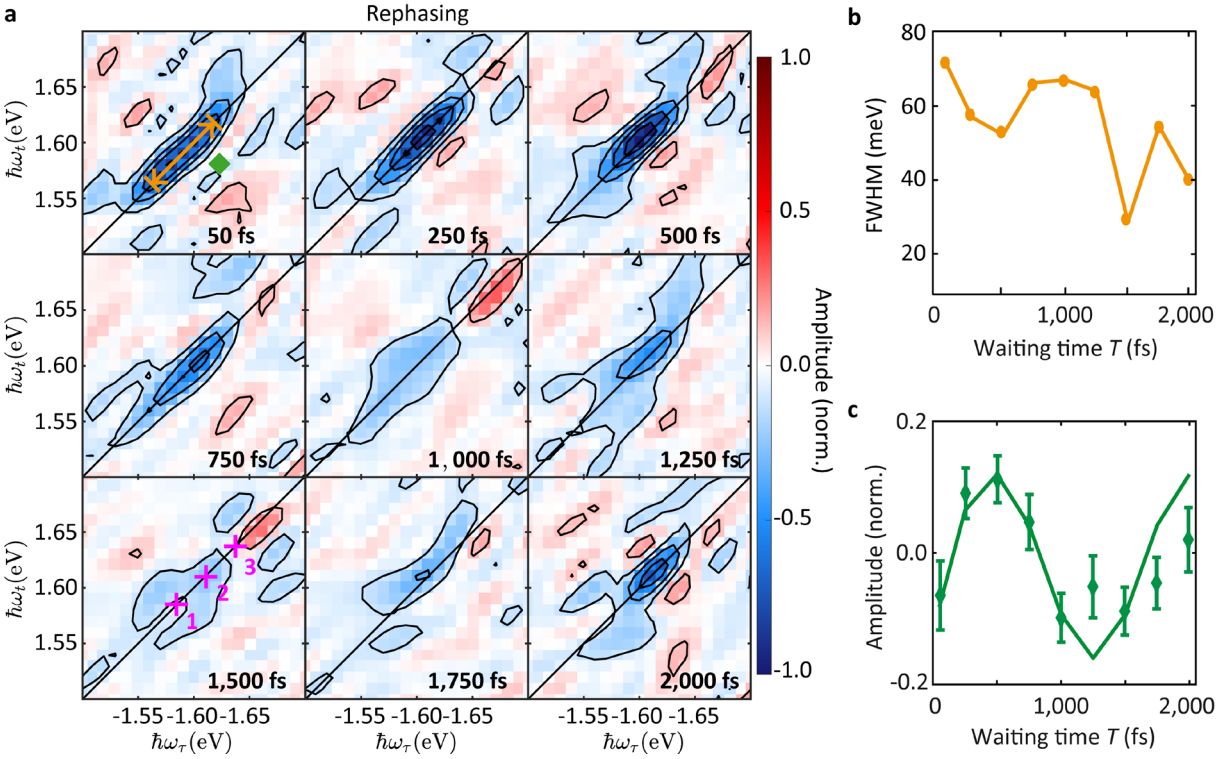

Figure 2 | Beating signal in the rephasing 2D maps. a, Rephasing 2D maps at different T, normalized to the maximum absolute value of the real part of the map at T = 500 fs. **b,** Diagonal linewidth (indicated by the orange double arrow at T = 50 fs in panel **a**) versus T. **c,** Amplitude evolution (green diamonds) of one pixel (marked by the green diamond at T = 50 fs in panel **a**) and fit (solid green curve). The error bars are evaluated by calculating the fluctuations within a region containing background noise (Supplementary Note 4).

The rephasing 2D maps in the region around the A exciton are shown in Fig. 2a for various *T*, while the nonrephasing and absorptive 2D maps are in Supplementary Figs. 1 and 5, respectively. The peak linewidth along the diagonal direction of the rephasing map (orange double arrow in upper left panel) is plotted versus *T* in Fig. 2b. Closer analysis of the systematic variation of this linewidth with *T* (Supplementary Note 2) indicates that there are 3 components along the diagonal, marked with purple crosses in the lower left panel of Fig. 2a, whose amplitudes oscillate, but not in phase. Thus, when *T*~1,500 fs, the amplitude of the middle component is much higher than the other two, minimizing the effective diagonal linewidth (minimum in Fig. 2b). The measured 2D maps capture the fourth-order nonlinear optical response, as sixth-order contributions are negligible (Supplementary Note 3).

We then extract the amplitude evolution of an exemplary pixel (marked by the green diamond in the 2D map at 50 fs) as a function of *T* (Fig. 2c). The number of points is restricted due to the long measurement time (26 h for one point). A long-lived (>2 ps) oscillation with amplitude above the noise level is observed. The reproducibility of the data is confirmed by a second measurement for the same *T* in Supplementary Note 4.

We now analyze the origin of the oscillations in the 2D maps with the goal to deduce the EXPC strength. Previous experiments reported that the trion signal in 1L-$MoSe_2$, located ~0.03 eV below the neutral exciton peak[54], gradually dies out both in PL and absorption when T increases from 15 to 295 K[25,54]. The electronic coupling between excitons and trions, observed at 20 K in Ref. 32, shows a dephasing time~250 fs. Thus, wave packets involving trions can be excluded as a source of the long-lived (>2 ps) RT oscillations in Fig. 2c. Vibrational wave packets were reported at RT in Ref. 21,22, with a dephasing time ~4.5 ps for 1L- and few-layer WSe_2[21] and ~1.7 ps for 1L-MoS_2[22]. Therefore, EXPC can explain the oscillations in our 2D maps. We extract the phonon energy from a fit (Fig. 2c, solid green curve) and obtain, even for our undersampled (less than one data point for each oscillation

period as a result of a compromise arising from finite available data acquisition time) data, an oscillation period ~136±2 fs (see Supplementary Note 5 for the fitting procedure). This corresponds to an energy splitting between the participating states~30.4±0.4 meV, matching the optical A'_1 phonon mode's energy~29.9 meV, i.e., 241 cm^{-1}, as measured in the Raman spectrum of Fig. 1d.

We define the EXPC strength using the Franck–Condon coupling model[55], with the minimum number of states needed to describe the observed data (Fig. 3a). We consider an electronic (or excitonic) ground state $|g\rangle$ and an electronic (or excitonic) first excited state $|e\rangle$. Using a harmonic oscillator to approximate the dependence of potential energy on a vibrational (phonon) dimensionless coordinate q with the ground-state minimum at $q = 0$ [55]:

$$V_g(q) = \frac{\hbar\omega}{2} q^2, \quad (1)$$

the potential curvature leads to a vibrational level spacing of $\hbar\omega$, where ω is the phonon angular frequency, creating sublevels $|g_i\rangle$, $i = 0, 1, 2, \ldots$. For full information on the system, we also need to describe the excited-state potential[55],

$$V_e(q) = \hbar\omega_{eg} + \frac{\hbar\omega}{2}(q + d)^2, \quad (2)$$

in which we assume, for simplicity, the same curvature, thus the same $\hbar\omega$ as in the ground state, a (vertical) energy difference $\hbar\omega_{eg}$, and a (horizontal) shift along the dimensionless phonon coordinate, d, between the two potential minima. This generates sublevels $|e_i\rangle$, $i = 0, 1, 2, \ldots$. Substituting Eq. 1 into Eq. 2 leads to:

$$V_e = \hbar\omega_{eg} + V_g + \hbar\omega S + \hbar\omega q d, \quad (3)$$

where $\hbar\omega S$ is the reorganization energy.

The model of Fig. 3a delivers 3 transition energies, as observed experimentally (purple crosses in Fig. 2a): We assign component 1 (with the lowest energy $\hbar\omega_1$) to the transition

between $|g_1\rangle$ and $|e_0\rangle$ (blue color in Fig. 3), component 2 (with a higher energy $\hbar\omega_2$) to the two degenerate transitions between $|g_0\rangle$ and $|e_0\rangle$ and between $|g_1\rangle$ and $|e_1\rangle$ (black and green colors, respectively), and component 3 (with the highest energy $\hbar\omega_3$) to the transition between $|g_0\rangle$ and $|e_1\rangle$ (red color).

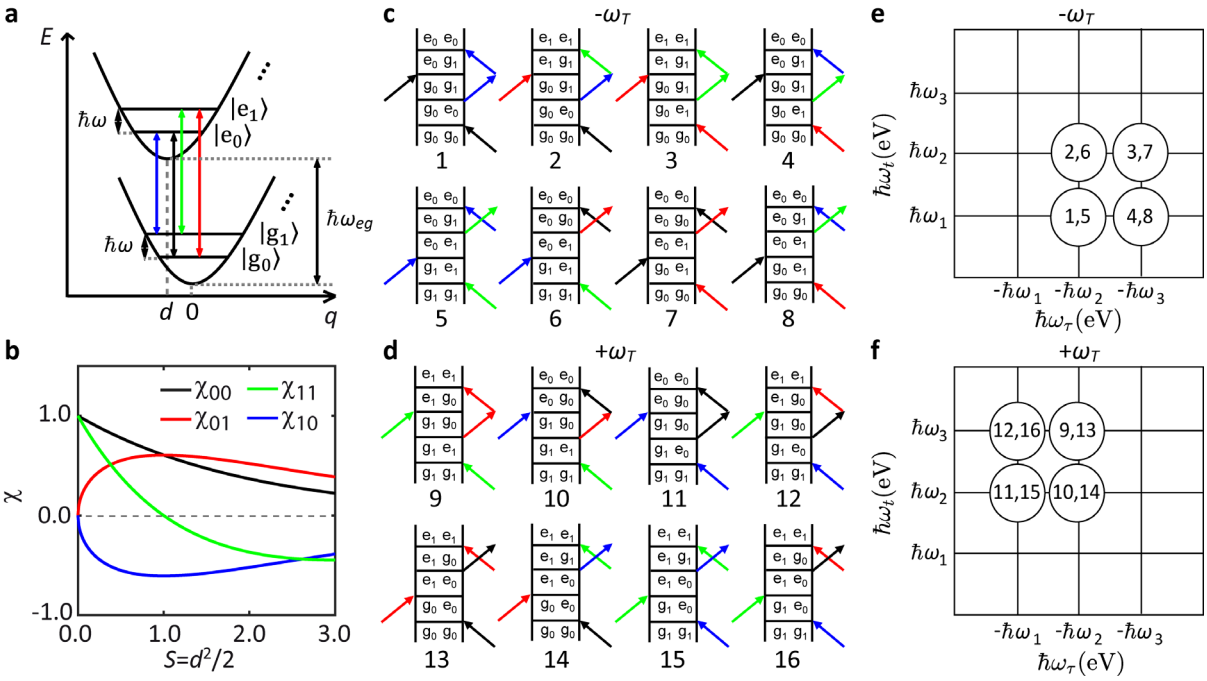

Figure 3 | Analysis of beating signals. a, Schematic diagram of displaced harmonic oscillators (Franck–Condon coupling model[55]) with two vibrational levels in the electronic ground state and two in the electronic excited state. **b,** Dependencies of Franck–Condon amplitudes χ_{ij} (i, j = 0 or 1) on S. **c,d,** Feynman pathways giving rise to the beating signals with (**c**) negative beating frequency $-\omega_T$ and (**d**) positive frequency $+\omega_T$. **e,** Beating-map locations of numbered Feynman pathways from panel **c. f,** Beating-map locations of numbered Feynman pathways from panel **d**. Transitions $|g_0\rangle$–$|e_0\rangle$, $|g_0\rangle$–$|e_1\rangle$, $|g_1\rangle$–$|e_0\rangle$, and $|g_1\rangle$–$|e_1\rangle$ are color-coded in black, red, blue, and green, respectively, for panels **a–d**.

Transitions between $|g_0\rangle$ and $|e_{i\geq 2}\rangle$ states are not observed in the 2D maps. This agrees with resonance Raman scattering[19,20] and their time-domain analogues[21,22], where the A'_1 overtone was not detected. This may imply an efficient nonradiative decay channel for the $|e_2\rangle$ state, which results in a fast dephasing time for the hot vibronic band transitions. Transitions between $|g_{i\geq 2}\rangle$ and $|e_0\rangle$ are also not observed in the 2D maps, which can be

explained as a negligible thermal population of $|g_{i\geq 2}\rangle$ due to a small Boltzmann factor at RT. The transition amplitudes between different vibronic sublevels (blue, black, green, and red arrows in Fig. 3a) are proportional to the overlap of the vibrational wave functions of initial and final state, i.e., the Franck–Condon amplitudes χ [56], plotted as a function of S in Fig. 3b. At $S = 0$, the red and blue curves are zero, indicating that it is not possible to excite $|e_1\rangle$ starting from $|g_0\rangle$ or to reach $|g_1\rangle$ from $|e_0\rangle$, thus the electronic/excitonic excitation is decoupled from vibrations.

We now correlate S with the oscillatory signals. We perform an additional Fourier transformation of 2D maps with respect to T. This gives rise to a three-dimensional (3D) spectrum, which is a hypercube as a function of $\hbar\omega_\tau$, $\hbar\omega_T$ and $\hbar\omega_t$.

Figure 3c lists all possible rephasing Feynman pathways that can result in contributions at negative beating frequency $-\omega_T$. Their individual positions in the 2D beating maps are in Fig. 3e. Figure 3d contains the contributions at positive ω_T, and Fig. 3f their positions in the 2D map. The peak position along the (horizontally displayed) $\hbar\omega_\tau$ excitation energy axis can be found by evaluating the energy difference between the states of the coherence created after the first light-field interaction. E.g., considering pathway 1, the first coherence created (and evolving with τ) is $|g_0\rangle\langle e_0|$. According to Fig. 3a (black arrow), this is located at the intermediate of the three possible transition energies for the excitation, i.e., at $\hbar\omega_2$, where the minus sign in Fig. 3e arises from the definition of sign of the frequency of a coherent state (a coherent state $|X\rangle\langle Y|$ has positive frequency when level $|X\rangle$ is higher in energy than level $|Y\rangle$ and negative frequency if level $|X\rangle$ is lower than $|Y\rangle$, see Supplementary Note 1). Likewise, the coherence after the third interaction (and evolving with t) is $|e_0\rangle\langle g_1|$, at the lowest of the 3 transition energies $\hbar\omega_1$ for the detection, according to the blue arrow in Fig. 3a with positive sign because $|e_0\rangle$ is higher than $|g_1\rangle$. All other peaks are assigned in a similar way, so that the displayed pattern emerges.

Adding all pathways, we expect the beating map to be located on the lower right of the diagonal for negative beating frequency (Fig. 3e), and on the upper left for positive (Fig. 3f). The precise shape of the overall beating map depends on the relative amplitudes of the individual Feynman pathways. Those depend on the initial populations of $|g_0\rangle$ and $|g_1\rangle$, hence on the sample temperature, and on the products of the Franck–Condon amplitudes of the 4 involved transitions (colored arrows in Figs. 3c,d) that in turn depend on S (Fig. 3b). Thus, analyzing the shape of the beating maps allows us to estimate S.

For a quantitative evaluation, we simulate the 2D beating maps by numerically solving a Lindblad master equation[57] for a system described by the Franck–Condon model illustrated in Fig. 3a (see Methods for details). S is varied from 0.25 to 2 with a step size of 0.25. Fig. 4a plots the simulation for S = 0.5, 1, and 1.5 from top to bottom. Data for other S are in Supplementary Fig. 13. We recognize the expected features of Figs. 3e,f. The pathway contributions overlap with each other, due to line broadening along the diagonal and anti-diagonal directions. For S = 1.5, the 4 underlying subpeaks create a square lineshape. For smaller S, the anti-diagonal linewidth changes strongly because of the varying relative contributions of the different Feynman pathways, leading to one asymmetric peak in each 2D beating map, whose center is located below (above) the diagonal line for negative (positive) beating frequency as predicted in Fig. 3e (Fig. 3f). The change in linewidth can be understood by considering that χ_{11} (Fig. 3b, solid green curve) crosses zero (the dashed gray line) for S = 1, such that only Feynman pathways 1, 7, 11, 13, e.g., without $|g_1\rangle$–$|e_1\rangle$ transition (green arrow in Figs. 3c,d), contribute. Therefore, the anti-diagonal linewidth reaches a minimum for S = 1.

Fig. 4b shows the experimental 2D beating maps at $-\omega_T$ (left) and $+\omega_T$ (right), obtained as cuts through the rephasing 3D spectrum at the same beating frequency as in the simulations, $\omega_T = 4.6 \times 10^{13}$ s^{-1}. The asymmetry with respect to the diagonal is visible, and the elliptical

shape [rather than roundish (small S) or squarish (large S)] points at an intermediate S by comparison with simulations.

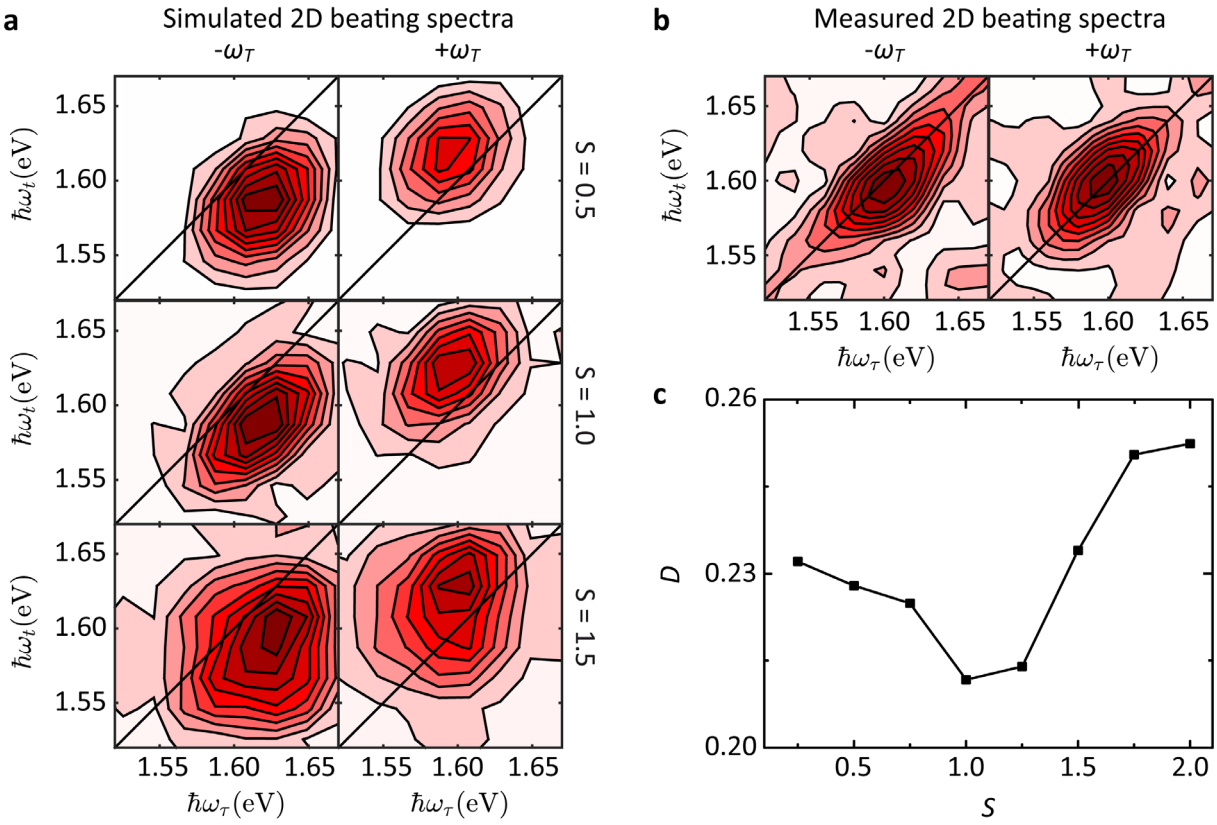

Figure 4 | 2D beating maps. a, Simulated 2D beating maps for $-\omega_T$ (left) and $+\omega_T$ (right) and S = 0.5, 1, 1.5 from top to bottom rows). **b,** Measured 2D beating maps with $-\omega_T$ (left) and $+\omega_T$ (right). **c,** The deviation, D, between measured and simulated 2D beating maps versus S used in the simulation.

To determine the EXPC strength quantitatively, we calculate the deviation D between measured and simulated 2D beating maps:

$$D = \sqrt{\frac{1}{N^2}\sum_{i=1}^{N}\sum_{j=1}^{N}\left(A_{ij}-\tilde{A}_{ij}\right)^2}, \quad (4)$$

where N is the pixel number in each dimension of the 2D beating maps, A_{ij} ($\tilde{A}_{ij}$) is the amplitude of the pixel in column i and row j of the simulated (experimental) 2D beating map. Figure 4c plots D versus S. We find the best agreement for $S = 1$. We then compare the experimental regular absorptive, rephasing, and nonrephasing 2D maps for T = 50 fs (Fig. 5a)

with the simulation using the optimal S (Fig. 5b) and find good agreement, confirming the reliability of our Franck–Condon model.

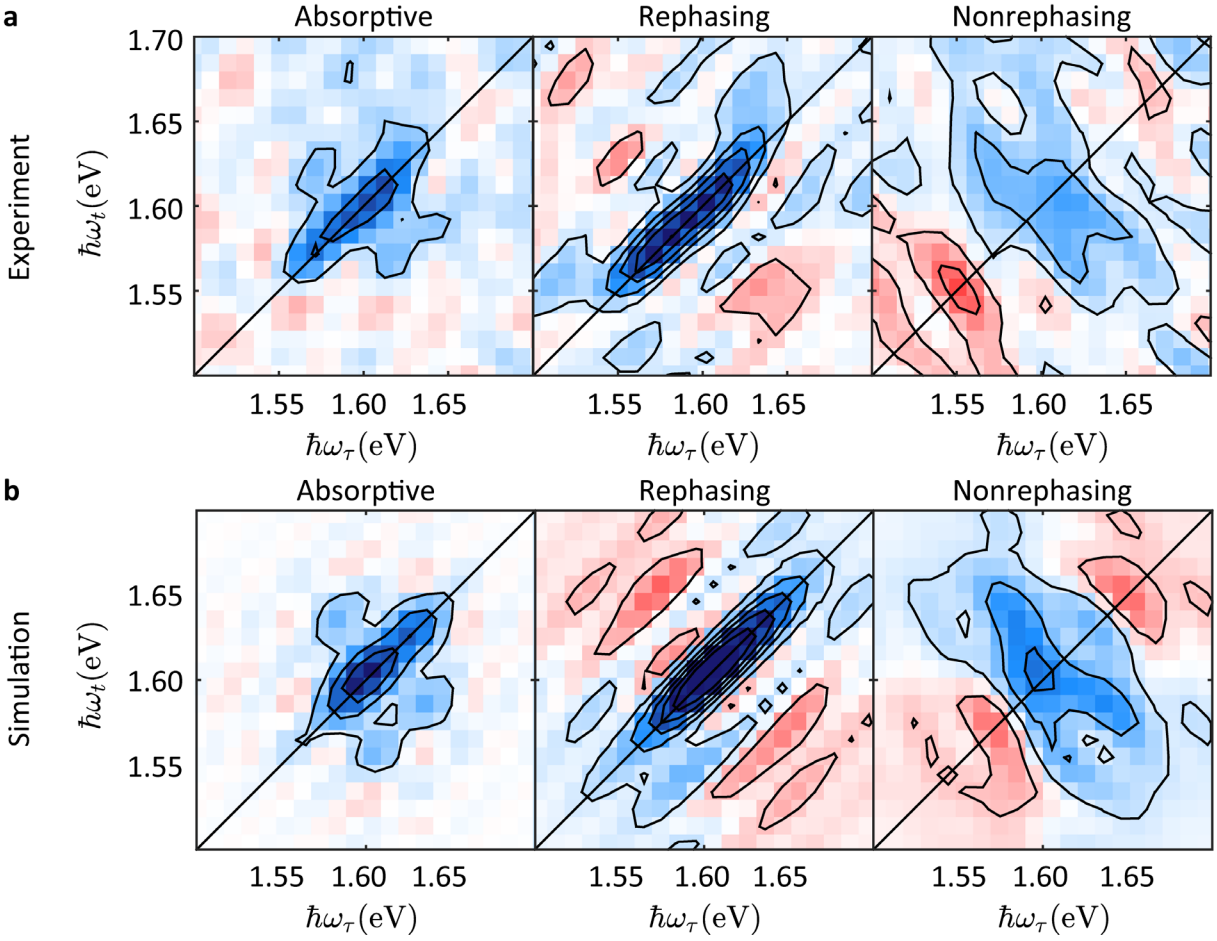

Figure 5 | Absorptive (left), rephasing (middle), and nonrephasing (right) real-valued 2D maps at T = 50 fs. a, Experiment. **b,** Simulation using the deduced optimal S = 1.

Conclusion

We carried out spatially resolved, fluorescence-detected 2D micro-spectroscopy on 1L-$MoSe_2$. We identified phonon sidebands upon excitation of the A exciton, due to coupling to the optical phonon mode A'$_1$. While the phonon is not resolved in linear absorption or PL spectra at room temperature, analysis of the 2D beating frequency as a function of waiting time allowed us to assign the phonon mode via comparison with Raman data. We determined the exciton–phonon coupling strength, i.e., the displacement along the phonon coordinate of the excited-exciton oscillator potential with respect to the ground state, and found a Huang–

Rhys factor, S~1, by comparison with simulations of 2D beating maps. The measured S~1 is larger than most reported values (S~0–0.5) of other inorganic semiconductor nanostructures[51], such as CdSe quantum dots[47] and rods[48], ZnSe quantum dots[49], single-wall carbon nanotubes[50], etc., indicating a strong EXPC. This finding may benefit, among others, the development of TMD-based polariton devices[58], in which the polariton-relaxation process strongly depends on the EXPC strength[59].

Our space-, time-, and excitation/detection-frequency-resolved spectroscopy provides a unique tool to measure EXPC strength also in other layered TMDs, and can be extended to other semiconducting systems for which phonon-induced subbands are expected in the excitonic lineshape, such as single-wall carbon nanotubes[60], layered perovskites[61], bulk heterojunctions[62], or other organic crystals. Because of the high spatial resolution of ~260 nm, our technique can also be used to study excitonic coupling in layered materials heterostructures or microcavities with embedded semiconductors. The determination of EXPC will provide design-relevant parameters for the development of photonic and optoelectronic devices based on these semiconducting systems.

Methods

Samples fabrication. The samples are prepared by micromechanical cleavage[63] of bulk $MoSe_2$ from HQ Graphene. Micromechanical cleavage is performed with polydimethylsiloxane (PDMS) and, after inspection under an optical microscope, 1L-$MoSe_2$ is dry transferred in ambient conditions to a 200 μm fused silica substrate[64]. After transfer, the samples are characterized by Raman and PL with a Renishaw Invia spectrometer at 514 nm and with a 50× objective. Metallic frames (Cr/Au) are fabricated around selected 1L-$MoSe_2$ flakes on fused silica by laser-writer lithography to facilitate the identification of the samples' position.

Data acquisition. A femtosecond oscillator (Venteon Laser Technologies GmbH, Pulse One PE) provides a laser spectrum ranging from 650 to 950 nm, confined by a hard aperture in the Fourier plane of a 4*f*-based pulse shaper in front of the liquid-crystal display (LCD, Jenoptik Optical Systems GmbH, SLM-S640d). The aperture acts as a short-pass filter at 808 nm, so that the longer-wavelength PL can be detected without scattering from the pump light. A Schott KG5 color filter further modulates the spectrum into a smooth shape, which ensures the absence of pronounced side peaks and other irregularities in the temporal pulse profile. The laser focus in the microscope is mapped by a piezo scanning stage (P-517.3CL, PI, Germany). Excitation occurs through a focusing objective (Nikon Plan Apo, 100×/1.40). PL is collected through the same objective, transmitted through a dichroic beam splitter (DBS, AHF Analysentechnik, F48-810) and an additional emission filter (EF, AHF Analysentechnik, F76-810), and detected by an APD (Perkin Elmer, SPCM-CD 2801).

Linearly polarized light, acting as a superposition of left- and right-hand circularly polarized light, is used to simultaneously excite both the transitions in the K and K' valleys. According to the relative band alignment, in Mo-based TMDs the intra-valley scattering processes are dominant over the inter-valley scatterings[9]. This allows us to model our system accounting just for the K valley, since the energy structures of the K and K' valleys are identical[65]. The pump fluence is ~2 μJ/cm^2.

We obtain the 2D maps by scanning τ and t in steps of 3 fs each from 0 to 99 fs, for T = 50, 250, 500, 750, 1000, 1250, 1500, 1750, 2000 fs, using the spectral modulation function[66]:

$$M(\omega) = \exp\left[i\left(\omega - \omega_0(1-\gamma)\right)(-\tau - T)\right] + \exp\left[i\left(\omega - \omega_0(1-\gamma)\right)(-T) + i\phi_{12}\right] + \exp[i\phi_{13}] + \exp\left[i\left(\omega - \omega_0(1-\gamma)\right)t + i\phi_{14}\right], \quad (5)$$

at a center frequency $\omega_0 = 2.5 \times 10^{15}\text{s}^{-1}$. We avoid undersampling with time steps of 3 fs by employing a partially rotating frame with γ = 0.2. The third pulse is fixed at time 0, so that

when 2D maps are measured at a certain T, only the first and fourth pulses are delayed. By setting the phase of the first pulse to 0, three relative phases, i.e., ϕ_{12}, ϕ_{13}, and ϕ_{14}, are scanned in a 27-step phase-cycling scheme, where each relative phase takes values of 0, $\frac{2\pi}{3}$, and $\frac{4\pi}{3}$. This allows us to select rephasing and nonrephasing contributions individually from the complete raw data[67,46]. We obtain absorptive 2D maps by summing the real parts of the rephasing and nonrephasing 2D maps, cancelling dispersion terms, leaving a pure absorptive lineshape[38]. Due to the finite response time of the liquid crystals of our pulse shaper, we wait ~500 ms after changing the phase mask before taking data. PL is averaged over ~1 ms for each APD acquisition period. Including additional averaging (1000 times for each pulse shape), the total measurement time for one 2D map is~26 h. The group delay dispersion at the sample position is compensated by adding an additional phase to the modulation function[46].

Simulations. To simulate the 2D maps, we solve the Lindblad quantum master equation[57]

$$\frac{\partial}{\partial t'}\rho(t') = -\frac{i}{\hbar}[\mathcal{H}(t'), \rho(t')] + \sum_j \frac{1}{T_j}\left(\mathcal{L}_j\rho(t')\mathcal{L}_j{}^{\dagger} - \frac{1}{2}\mathcal{L}_j{}^{\dagger}\mathcal{L}_j\rho(t') - \frac{1}{2}\rho(t')\mathcal{L}_j\mathcal{L}_j{}^{\dagger}\right), \qquad (6)$$

where the time evolution of the density matrix $\rho(t')$ of the quantum system under a Hamiltonian $\mathcal{H}(t')$ is treated in the Liouville–von Neumann formalism, with the extension of dissipative and pure dephasing effects, $\mathcal{H}(t')$ is expressed as the sum of a time-independent Hamiltonian $\mathcal{H}_0 = \hbar\omega_m\sum_m|m\rangle\langle m|$ and an interaction Hamiltonian $\mathcal{H}_I(t') = \gamma_{\mathrm{ex}}\,E(t')\sum_{m\neq n}\mu_{m,n}(|m\rangle\langle n| + |n\rangle\langle m|)$, where $|m\rangle$ (or $|n\rangle$) are the unperturbed eigenstates with eigenenergies $\hbar\omega_m$ (or $\hbar\omega_n$), γ_{ex} is the field coupling strength for excitation with the external electric field $E(t')$, $\mu_{m,n}$ is the transition dipole moment between states $|m\rangle$ and $|n\rangle$, T_j represents the time associated with a pure dephasing or population relaxation process, and the Lindblad operators $\mathcal{L}_j$ are defined as $\mathcal{L}_j = a_n^{\dagger}a_n$ for pure dephasing and $\mathcal{L}_j = a_m^{\dagger}a_n$ with $m \neq n$ for a population relaxation process, where $a_m^{\dagger}$ and a_n denote the creation and annihilation operators, respectively.

We assume a four-level system, with two vibrational levels in the ground electronic state ($|g_0\rangle$ and $|g_1\rangle$) and two vibronically excited states ($|e_0\rangle$ and $|e_1\rangle$), as in Fig. 3a. The splittings within the subbands are taken to be identical, i.e., we use the same energy separations (30 meV[21]) between $|g_0\rangle$ and $|g_1\rangle$ as well as between $|e_0\rangle$ and $|e_1\rangle$. The Franck–Condon amplitudes between $|g_i\rangle$ and $|e_j\rangle$, i.e., χ_{ij} (i, j = 0 or 1) depend on S as for Fig. 3b. The initial populations of $|g_0\rangle$ and $g_1\rangle$ are determined by the temperature, according to the Boltzmann distribution. In Supplementary Note 7 we estimate the heating through laser irradiation during the experiment and find the sample to remain close to RT.

The excitation laser field is calculated from the experimentally utilized laser spectrum assuming a flat phase and then adding the transfer function:

$$M(\omega) = \exp\left[i\left(\omega - \omega_0(1-\gamma)\right)(T_{\text{off}})\right] + \exp\left[i\left(\omega - \omega_0(1-\gamma)\right)(T_{\text{off}} + \tau) + i\phi_{12}\right] + \exp\left[i\left(\omega - \omega_0(1-\gamma)\right)(T_{\text{off}} + \tau + T) + i\phi_{13}\right] + \exp\left[i\left(\omega - \omega_0(1-\gamma)\right)(T_{\text{off}} + \tau + T + t) + i\phi_{14}\right], \quad (7)$$

where T_{off} is an offset of the position of the first pulse in time domain, set at 100 fs to avoid cutting off the first pulse at time zero. In the experimental modulation function of Eq. 5, time zero is set at the maximum of the third pulse, leading to a different mathematical expression. However, this difference does not affect the resulting 2D maps, since only relative time delays between the pulses are relevant. τ and t in the simulation are scanned with the same parameters as in the experiment, from 0 to 99 fs in steps of 3 fs with γ = 0.2, whereas T is scanned from 0 to 200 fs in steps of 25 fs.

Inhomogeneous broadening due to a Gaussian distribution of excitonic transition frequencies is taken into account by obtaining the inhomogeneously broadened response function, $S_I(\tau, t)$, from the homogeneous response, $S(\tau, t)$. From solving Eq. 6, via:

$$S_I(\tau, t) = S(\tau, t) \cdot \exp[-\Delta^2 \cdot (\tau \mp t)^2], \quad (8)$$

where Δ is a parameter linearly proportional to the inhomogeneous linewidth broadening, - is applied for the rephasing signal, and + for the nonrephasing signal. Eq. 8 is used under two assumptions. 1) Spectral diffusion can be ignored within the T = 2 ps window of the measurements. Typically, spectral diffusion is caused by environmental fluctuations around the transition dipoles, inducing a broadening along the anti-diagonal direction for the absorptive 2D maps as T increases[38]. This is not observed in our experiments (Supplementary Figure 5), indicating a much slower than 2 ps modulation time constant of the environment, justifying the use of Eq. 8. 2) The vibrational frequency does not change with the excitonic transition energy, also assumed for the model of Fig. 3a and Eqs. 1–3. If this was not fulfilled, a tilt of elongated peaks in the 2D beating maps relative to the diagonal would be observed[40], unlike in our measurements (Fig. 4b).

Data availability

The data that support the findings of this study are available from the corresponding author upon reasonable request.

Acknowledgements

We thank Pavel Malý for support with computations of 2D maps. We acknowledge funding by the European Research Council (ERC) – Grants No. 614623, Hetero2D, GSYNCOR; EPSRC Grants EP/K01711X/1, EP/K017144/1, EP/N010345/1, and EP/L016087/1; and the EU Graphene and Quantum Flagships.

Author contributions

D.L., C.T., and M.N. performed spectroscopic measurements. D.L. analyzed the 2DES data and conducted the 2DES simulations. S.D.C. supervised C.T.; T.B., G.C. and A.C.F. initiated and supervised the project. G.S. and G.W. prepared and characterized the samples. All authors

discussed results. D.L., C.T., G.C., T.B. and A.C.F. wrote the paper with input from all coauthors.

Competing interests

The authors declare no competing interests.

Additional information

Supplementary information is available for this paper.

References

1. Bonaccorso, F., Sun, Z., Hasan, T. & Ferrari, A. C. Graphene photonics and optoelectronics. *Nat. Photonics* **4**, 611–622 (2010).
2. Koppens, F. H. L. *et al.* Photodetectors based on graphene, other two-dimensional materials and hybrid systems. *Nat. Nanotechnol.* **9**, 780–793 (2014).
3. C. Ferrari, A. *et al.* Science and technology roadmap for graphene, related two-dimensional crystals, and hybrid systems. *Nanoscale* **7**, 4598–4810 (2015).
4. Romagnoli, M. *et al.* Graphene-based integrated photonics for next-generation datacom and telecom. *Nat. Rev. Mater.* **3**, 392 (2018).
5. Splendiani, A. *et al.* Emerging photoluminescence in monolayer MoS_2. *Nano Lett.* **10**, 1271–1275 (2010).
6. Mak, K. F., Lee, C., Hone, J., Shan, J. & Heinz, T. F. Atomically thin MoS_2: A new direct-gap semiconductor. *Phys. Rev. Lett.* **105**, 136805 (2010).
7. Qiu, D. Y., da Jornada, F. H. & Louie, S. G. Optical spectrum of MoS_2: Many-body effects and diversity of exciton states. *Phys. Rev. Lett.* **111**, 216805 (2013).
8. Chernikov, A. *et al.* Exciton binding energy and nonhydrogenic Rydberg series in monolayer WS_2. *Phys. Rev. Lett.* **113**, (2014).

9. Selig, M. *et al.* Excitonic linewidth and coherence lifetime in monolayer transition metal dichalcogenides. *Nat. Commun.* **7**, 13279 (2016).
10. Jakubczyk, T. *et al.* Impact of environment on dynamics of exciton complexes in a WS_2 monolayer. *2D Mater.* **5**, 031007 (2018).
11. Yuan, L. & Huang, L. Exciton dynamics and annihilation in WS_2 2D semiconductors. *Nanoscale* **7**, 7402–7408 (2015).
12. Paradisanos, I. *et al.* Efficient phonon cascades in hot photoluminescence of WSe_2 monolayers. *arXiv:2007.05369* (2020).
13. Yuan, L. & Huang, L. Exciton dynamics and annihilation in WS_2 2D semiconductors. *Nanoscale* **7**, 7402–7408 (2015).
14. Li, Z. *et al.* Emerging photoluminescence from the dark-exciton phonon replica in monolayer WSe_2. *Nat. Commun.* **10**, 2469 (2019).
15. Wang, Z. *et al.* Intravalley spin–flip relaxation dynamics in single-layer WS_2. *Nano Lett.* **18**, 6882–6891 (2018).
16. Moody, G. *et al.* Intrinsic homogeneous linewidth and broadening mechanisms of excitons in monolayer transition metal dichalcogenides. *Nat. Commun.* **6**, 8315 (2015).
17. Shree, S. *et al.* Observation of exciton-phonon coupling in $MoSe_2$ monolayers. *Phys. Rev. B* **98**, 035302 (2018).
18. Christiansen, D. *et al.* Phonon sidebands in monolayer transition metal dichalcogenides. *Phys. Rev. Lett.* **119**, 187402 (2017).
19. Soubelet, P., Bruchhausen, A. E., Fainstein, A., Nogajewski, K. & Faugeras, C. Resonance effects in the Raman scattering of monolayer and few-layer $MoSe_2$. *Phys. Rev. B* **93**, 155407 (2016).
20. Carvalho, B. R., Malard, L. M., Alves, J. M., Fantini, C. & Pimenta, M. A. Symmetry-dependent exciton-phonon coupling in 2D and bulk MoS_2 observed by resonance Raman scattering. *Phys. Rev. Lett.* **114**, 136403 (2015).
21. Jeong, T. Y. *et al.* Coherent lattice vibrations in mono- and few-layer WSe_2. *ACS Nano* **10**, 5560–5566 (2016).

22. Trovatello, C. *et al.* Strongly coupled coherent phonons in single-layer MoS_2. *ACS Nano* (2020) doi:10.1021/acsnano.0c00309.
23. Webb, M. D., Cundiff, S. T. & Steel, D. G. Stimulated-picosecond-photon-echo studies of localized exciton relaxation and dephasing in GaAs/$Al_xGa_{1-x}As$ multiple quantum wells. *Phys. Rev. B* **43**, 12658–12661 (1991).
24. Fischer, A. J. *et al.* Femtosecond four-wave-mixing studies of nearly homogeneously broadened excitons in GaN. *Phys. Rev. B* **56**, 1077–1080 (1997).
25. Scarpelli, L. *et al.* Resonantly excited exciton dynamics in two-dimensional $MoSe_2$ monolayers. *Phys. Rev. B* **96**, 045407 (2017).
26. Kosarev, A. N. *et al.* Microscopic dynamics of electron hopping in a semiconductor quantum well probed by spin-dependent photon echoes. *Phys. Rev. B* **100**, 121401 (2019).
27. Poltavtsev, S. V. *et al.* Polarimetry of photon echo on charged and neutral excitons in semiconductor quantum wells. *Sci. Rep.* **9**, 1–9 (2019).
28. Turner, D. B., Wilk, K. E., Curmi, P. M. G. & Scholes, G. D. Comparison of electronic and vibrational coherence measured by two-dimensional electronic spectroscopy. *J. Phys. Chem. Lett.* **2**, 1904–1911 (2011).
29. Butkus, V., Zigmantas, D., Valkunas, L. & Abramavicius, D. Vibrational vs. electronic coherences in 2D spectrum of molecular systems. *Chem. Phys. Lett.* **545**, 40–43 (2012).
30. Song, Y., Clafton, S. N., Pensack, R. D., Kee, T. W. & Scholes, G. D. Vibrational coherence probes the mechanism of ultrafast electron transfer in polymer–fullerene blends. *Nat. Commun.* **5**, 4933 (2014).
31. Thyrhaug, E. *et al.* Identification and characterization of diverse coherences in the Fenna–Matthews–Olson complex. *Nat. Chem.* **10**, 780–786 (2018).
32. Hao, K. *et al.* Coherent and incoherent coupling dynamics between neutral and charged excitons in monolayer $MoSe_2$. *Nano Lett.* **16**, 5109–5113 (2016).

33. Tempelaar, R. & Berkelbach, T. C. Many-body simulation of two-dimensional electronic spectroscopy of excitons and trions in monolayer transition metal dichalcogenides. *Nat. Commun.* **10**, 1–7 (2019).
34. Mukamel, S. Multidimensional femtosecond correlation spectroscopies of electronic and vibrational excitations. *Annu. Rev. Phys. Chem.* **51**, 691–729 (2000).
35. Jonas, D. M. Two-dimensional femtosecond spectroscopy. *Annu. Rev. Phys. Chem.* **54**, 425–463 (2003).
36. Cho, M. Coherent two-dimensional optical spectroscopy. *Chem. Rev.* **108**, 1331–1418 (2008).
37. Ginsberg, N. S., Cheng, Y.-C. & Fleming, G. R. Two-dimensional electronic spectroscopy of molecular aggregates. *Acc. Chem. Res.* **42**, 1352–1363 (2009).
38. Hamm, P. & Zanni, M. *Concepts and methods of 2D infrared spectroscopy*. (Cambridge University Press, 2011).
39. Christensson, N., Kauffmann, H. F., Pullerits, T. & Mančal, T. Origin of long-lived coherences in light-harvesting complexes. *J. Phys. Chem. B* **116**, 7449–7454 (2012).
40. Seibt, J. & Pullerits, T. Beating signals in 2D spectroscopy: Electronic or nuclear coherences? Application to a quantum dot model system. *J. Phys. Chem. C* **117**, 18728–18737 (2013).
41. Tiwari, V. *et al.* Spatially-resolved fluorescence-detected two-dimensional electronic spectroscopy probes varying excitonic structure in photosynthetic bacteria. *Nat. Commun.* **9**, 4219 (2018).
42. Tian, P., Keusters, D., Suzaki, Y. & Warren, W. S. Femtosecond phase-coherent two-dimensional spectroscopy. *Science* **300**, 1553–1555 (2003).
43. Tekavec, P. F., Lott, G. A. & Marcus, A. H. Fluorescence-detected two-dimensional electronic coherence spectroscopy by acousto-optic phase modulation. *J. Chem. Phys.* **127**, 214307 (2007).
44. Tan, H.-S. Theory and phase-cycling scheme selection principles of collinear phase coherent multi-dimensional optical spectroscopy. *J. Chem. Phys.* **129**, 124501 (2008).
45. Aeschlimann, M. *et al.* Coherent two-dimensional nanoscopy. *Science* **333**, 1723–1726 (2011).

46. Goetz, S., Li, D., Kolb, V., Pflaum, J. & Brixner, T. Coherent two-dimensional fluorescence micro-spectroscopy. *Opt. Express* **26**, 3915–3925 (2018).
47. Baker, J. A., Kelley, D. F. & Kelley, A. M. Resonance Raman and photoluminescence excitation profiles and excited-state dynamics in CdSe nanocrystals. *J. Chem. Phys.* **139**, 024702 (2013).
48. Lange, H. *et al.* Optical phonons in colloidal CdSe nanorods. *Phys. Status Solidi B* **247**, 2488–2497 (2010).
49. Gong, K., Kelley, D. F. & Kelley, A. M. Resonance Raman spectroscopy and electron–phonon coupling in Zinc Selenide quantum dots. *J. Phys. Chem. C* **120**, 29533–29539 (2016).
50. Lüer, L. *et al.* Coherent phonon dynamics in semiconducting carbon nanotubes: A quantitative study of electron-phonon coupling. *Phys. Rev. Lett.* **102**, 127401 (2009).
51. Kelley, A. M. Exciton-optical phonon coupling in II-VI semiconductor nanocrystals. *J. Chem. Phys.* **151**, 140901 (2019).
52. Li, Y. *et al.* Measurement of the optical dielectric function of monolayer transition-metal dichalcogenides: MoS_2, $MoSe_2$, WS_2, and WSe_2. *Phys. Rev. B* **90**, 205422 (2014).
53. Tonndorf, P. *et al.* Photoluminescence emission and Raman response of monolayer MoS_2, $MoSe_2$, and WSe_2. *Opt. Express* **21**, 4908–4916 (2013).
54. Ross, J. S. *et al.* Electrical control of neutral and charged excitons in a monolayer semiconductor. *Nat. Commun.* **4**, 1474 (2013).
55. Mukamel, S. *Principles of nonlinear optical spectroscopy*. (Oxford University Press, 1995).
56. van Amerongen, H., Valkunas, L. & van Grondelle, R. *Photosynthetic Excitons*. (World Scientific Publishing Co. Pte. Ltd., 2000).
57. Lindblad, G. On the generators of quantum dynamical semigroups. *Commun. Math. Phys.* **48**, 119–130 (1976).
58. Schneider, C., Glazov, M. M., Korn, T., Höfling, S. & Urbaszek, B. Two-dimensional semiconductors in the regime of strong light-matter coupling. *Nat. Commun.* **9**, 2695 (2018).
59. Coles, D. M. *et al.* Vibrationally assisted polariton-relaxation processes in strongly coupled organic-semiconductor microcavities. *Adv. Funct. Mater.* **21**, 3691–3696 (2011).

60. Murakami, Y. *et al.* Photoluminescence sidebands of carbon nanotubes below the bright singlet excitonic levels. *Phys. Rev. B* **79**, 195407 (2009).
61. Mauck, C. M. & Tisdale, W. A. Excitons in 2D organic–inorganic halide perovskites. *Trends Chem.* **1**, 380–393 (2019).
62. Street, R. A. Electronic structure and properties of organic bulk-heterojunction interfaces. *Adv. Mater.* **28**, 3814–3830 (2016).
63. Novoselov, K. S. *et al.* Two-dimensional atomic crystals. *Proc. Natl. Acad. Sci.* **102**, 10451–10453 (2005).
64. Bonaccorso, F. *et al.* Production, processing and placement of graphene and two dimensional crystals. *Mater. Today* **15**, 564 (2012).
65. Xiao, D., Liu, G.-B., Feng, W., Xu, X. & Yao, W. Coupled spin and valley physics in monolayers of MoS_2 and other group-VI dichalcogenides. *Phys. Rev. Lett.* **108**, 196802 (2012).
66. Galler, A. & Feurer, T. Pulse shaper assisted short laser pulse characterization. *Appl. Phys. B Lasers Opt.* **90**, 427–430 (2008).
67. Draeger, S., Roeding, S. & Brixner, T. Rapid-scan coherent 2D fluorescence spectroscopy. *Opt. Express* **25**, 3259–3267 (2017).